https://doi.org/10.5194/egusphere-2026-3347
Preprint. Discussion started: 11 August 2026

Volcanic eruptions alter sky colours in a geoengineered world

Anna Lange [1], Ilaria Quaglia [2], Daniele Visioni [3], Alexei Rozanov [4], and Christian von Savigny [1]

[1]Institute of Physics, University of Greifswald, Felix-Hausdorff-Str. 6, 17489 Greifswald, Germany
[2]NSF National Center for Atmospheric Research, Boulder, CO, USA
[3]Department of Earth and Atmospheric Sciences, Cornell University, Ithaca, NY, 14850 USA
[4]Institute of Environmental Physics, University of Bremen, Otto-Hahn-Allee 1, 27359 Bremen, Germany

Correspondence: Anna Lange (anna.lange@uni-greifswald.de)

Abstract. This study examines sky colour changes in a geoengineered world following a volcanic eruption, combining CESM2-(WACCM6) climate model simulations, SCIATRAN radiative transfer calculations, and colour modelling. Bridging a gap in existing research, this is the first study to analyse how sky colours respond when a volcanic eruption occurs in the context of an ongoing stratospheric aerosol injection (SAI) deployment. The SAI experiments consist of simulations with feedback-controlled sulphur dioxide injections amounting to 7.5 Tg per year at the time of the volcanic eruption, with eruption magnitudes of 10 and 50 Tg sulphur dioxide. The results show several optical phenomena, including Bishop's Rings near the solar horizon, anomalous greenish twilight colouration, and pronounced purple light. The latter is consistent with prior findings linking vivid purple colours to elevated aerosol loading. Despite variations in SAI scenario design, with Northern Hemisphere suspension in one scenario and complete suspension in the other, no significant differences in sky colour were found between the scenarios, months, and latitude investigated following the volcanic eruption with a magnitude of 10 Tg sulphur dioxide.

1 Introduction

Stratospheric aerosol injections (SAI) have been suggested as one possible approach for reducing specific effects of climate change, including the increase in global average temperatures (Budyko, 1977; Crutzen, 2006). This idea is inspired by the natural cooling effect observed after explosive volcanic eruptions, which release large amounts of sulphur dioxide into the stratosphere. SAI remains subject to substantial scientific and societal debate due to unresolved research gaps and uncertainties (e.g., Haywood et al., 2025; Eastham et al., 2025). At the same time, ongoing climate change and rising associated damages and costs continue to drive discussions of possible deployment scenarios.

Large volcanic eruptions, the natural analogue of SAI, can significantly alter the colour of the sky, particularly at twilight, for months or even years by enhancing stratospheric aerosol loading. Under such conditions, the usual sunset colours may be accompanied by a secondary afterglow that persists much longer than ordinary twilight colours (Meinel and Meinel, 1991) as well as intense red, purple, or greenish hues can occur (Symons et al., 1888). In addition, volcanic aerosol loading can produce blue or green colouring of the Sun (e.g., Wullenweber et al., 2021). A prominent historical example is the 1883 Krakatoa eruption, following which exceptionally intense sky colours were documented (Symons et al., 1888), and the optical phenomenon known as Bishop's Ring, a broad diffuse corona around the Sun, was first described (Symons et al., 1888).

https://doi.org/10.5194/egusphere-2026-3347
Preprint. Discussion started: 11 August 2026

There are currently two studies, to the best of our knowledge, examining changes in sky colour following SAI (Kravitz et al., 2012; Lemon et al., 2025). Kravitz et al. (2012) simulated irradiance spectra for an observer on the Earth's surface under sulphate-based SAI for the day and sunset with aerosol loadings that correspond to up to a 2 % reduction in irradiance received at the Earth's surface. Kravitz et al. (2012) concluded that the additional sulphate layer would produce sky colours similar to those observed after volcanic eruptions, including daytime sky whitening, sunset afterglows, and a general increase in sky brightness or diffuse irradiance. In contrast, Lemon et al. (2025) analysed the visual impacts of SAI, including visibility, for different aerosol types (sulphuric acid, calcite, and diamond). Lemon et al. (2025) demonstrate that moderate SAI (-1 – -2 W/m^2 radiative forcing) would leave the daytime skies nearly unchanged for most observers. Enhanced brightness mostly emerges during twilight, but remaining below human perceptual thresholds (Lemon et al., 2025).

If SAI were ever deployed, volcanic eruptions would continue to occur naturally and intermittently perturb the stratospheric aerosol burden. Consequently, periods of background SAI aerosol loading and episodic volcanic aerosol enhancements would likely coexist. Understanding how these combined aerosol perturbations can influence the colours of the sky and atmospheric appearance is therefore relevant for assessing the visual and perceptual consequences of a geoengineered atmosphere.

Bridging a gap in existing research, the current study is the first to analyse sky colours after volcanic eruptions in SAI conditions, with a particular focus on whether volcanic eruptions can further exacerbate sky colour change in a geoengineered world for different SAI scenarios. CESM2(WACCM6) model simulations, SCIATRAN radiative transfer simulations, and subsequent colour modelling are applied to investigate these questions.

The paper is structured as follows. Section 2 introduces the relevant methods, such as the CESM2(WACCM6) Earth System Model, the radiative transfer model SCIATRAN, and the colour modelling approach. Section 3 illustrates the results, followed by the discussion and conclusions.

2 Methodology

2.1 CESM2(WACCM6) Earth System Model

Particle size information for the different scenarios is derived from model simulations using the Community Earth System Model, version 2, with the Whole Atmosphere Community Climate Model version 6 as the atmospheric component, CESM2(WACCM6) (Gettelman et al., 2019; Danabasoglu et al., 2020). The Earth System Model comprises interactively coupled atmosphere, ocean, land, and sea ice components. With a horizontal resolution of 0.95° latitude × 1.25° longitude, and 70 vertical layers extending up to 140 km, the model adequately resolves internal variability in the stratosphere.

The WACCM6-MA configuration employed in this study includes Middle-Atmosphere chemistry, accounting for stratospheric species and reactions (Mills et al., 2017; Davis et al., 2023). Aerosols are simulated using the Modal Aerosol Model version 4 (MAM4), extended to include prognostic stratospheric sulphate aerosols, that includes black carbon, primary organic matter, secondary organic aerosols, sea salt, dust, and sulphate internally mixed in four log-normal modes: Primary carbon, Aitken, Accumulation, and Coarse mode (Liu et al., 2016).

https://doi.org/10.5194/egusphere-2026-3347
Preprint. Discussion started: 11 August 2026

The simulations of volcanic eruptions and SAI were conducted under the Shared Socioeconomic Pathway 2–4.5 (Meinshausen et al., 2020) (SSP2-4.5), which serves as a background greenhouse gas and anthropogenic aerosols emission scenario (MacMartin et al., 2022).

The SAI experiments consist of 35-year simulations initialised in 2035, with annually constant sulphur dioxide (SO_2) injections at four latitudes: 30° N, 15° N, 15° S, and 30° S at 180° E longitude in a grid box centred at 21.5 km altitude with a vertical resolution of 1.2 km. The injection rates were controlled by a feedback algorithm that maintains the global mean temperature at 1.5° above the pre-industrial level, defined as the average over the 2020 – 2039 period in CESM2, as well as the inter-hemispheric and equator to pole temperature gradients (Kravitz et al., 2016; MacMartin et al., 2022). At the time of the volcanic eruption (1 January 2055), the SAI injection rate amounts to 7.5 Tg SO_2/yr, with 74 % located in the southern hemisphere (SH) and 26 % located in northern hemisphere (NH), yielding mean stratospheric aerosol optical depth (SAOD) values of 0.16 (SH) and 0.10 (NH) at 550 nm. The volcanic eruptions were represented as injections uniformly distributed between 18 and 25 km altitude, centred at the location of Mt. Pinatubo (15.1° N, 120.4° E). For more details we refer to Quaglia et al. (2024). All studies were conducted for the latitude of 15° N, as the greatest effects are expected at this latitude, focusing on month one (time of the volcanic eruption) and month five (when the global sulphate burden and SAOD reach their maximum).

The investigated scenarios are listed in the following Tab. 1.

Table 1. Description of the scenarios examined in this study. The scenarios follow the investigations in Quaglia et al. (2024).

Scenario	**Scenario description**
1. SAI	SAI without volcanic eruption.
2. Volc10Tg + SAI_nhoff	Volcanic eruption (10 Tg SO_2) under SAI. After the eruption SAI is suspended for 2 years in NH and maintained in SH.
3. Volc10Tg + SAI_off	Volcanic eruption (10 Tg SO_2) under SAI. SAI is immediately stopped everywhere when the eruption occurs.
4. Volc50Tg + SAI_off	Volcanic eruption (50 Tg SO_2) under SAI. SAI is immediately stopped everywhere when the eruption occurs.

2.2 SCIATRAN radiative transfer model

All radiative transfer simulations presented in this work were carried out using the radiative transfer model SCIATRAN version 4.5.5 with implemented Mie code (Rozanov et al., 2014). SCIATRAN was run in the approximate spherical mode, i.e., an approximate treatment of the multiple scattering is performed, while the contribution of single scattering is calculated in a fully spherical geometry (Rozanov et al., 2000). As shown by Lange et al. (2022), this approximation proves to be sufficient for the simulations carried out here.

Atmospheric trace gas, temperature and pressure profiles were taken from a climatological database obtained from a 3-D chemical transport model (Sinnhuber et al., 2003). Refraction effects are accounted for both direct and scattered sunlight.

https://doi.org/10.5194/egusphere-2026-3347
Preprint. Discussion started: 11 August 2026

Output of the SCIATRAN simulations performed here are radiances for a wavelength range of 380 – 800 nm. The simulated radiances represent scattered solar radiation, not directly transmitted sunlight. To derive the spectral distribution of scattered solar radiation as seen by a ground-based observer, a solar irradiance spectrum from SORCE (Solar Radiation and Climate Experiment) measurements (LASP, 2003) was used.

For the implemented stratospheric sulphate aerosols, monthly mean particle size information (see Fig. A1 for the effective radius) from the CESM2(WACCM6) simulations from the corresponding scenario of the accumulation and coarse modes were used. Therefore, a bimodal distribution with two log-normal modes was assumed:

$$n(r) = \frac{N_0}{\sqrt{2\pi}\cdot\ln(S)\cdot r}\cdot\exp\left[-\frac{(\ln r - \ln r_m)^2}{2\ln^2(S)}\right], \tag{1}$$

here N_0 is the particle number density of each of the two modes, r_m the median radius, r the particle radius and S the geometric standard deviation of the distribution.

The simulations were performed for solar zenith angles (SZAs) of 90 – 98°, in 2° steps, solar azimuth angles (SAAs), which describe the azimuth angle of the Sun's position with respect to the viewing direction (value of 0° corresponds to the solar direction, and the value of 180° to the anti-solar direction), of 0 – 180°, in 2° steps, and for viewing zenith angles (VZAs) of 0 – 90°, in 2° steps. The viewing zenith angle describes the line-of-sight angle at the observer's location, with a maximum of 90° for a ground-based observer. At 0°, the observer is looking directly at the zenith. At 90°, the line of sight lies along the horizon (see Fig. A2). These angles were chosen because they cover, on the one hand, the entire range from the horizon to the zenith, and on the other hand, the entire solar azimuthal range from the solar side to the anti-solar side. Furthermore, the SZA was selected to cover precisely the period of sunset and the subsequent twilight, when the greatest effects are expected.

2.3 Colour modelling

The International Commission on Illumination (CIE) 1931 XYZ colour system (CIE, 2004) was used to represent the colours based on the simulated scattered solar spectra. For this purpose, the simulated spectrum $I(\lambda)$ was weighted with the CIE colour matching functions $\overline{x}(\lambda)$, $\overline{y}(\lambda)$ and $\overline{z}(\lambda)$, which describe the spectral sensitivity of the cone cells of the human eye. The Y component corresponds to the CIE luminance and serves as the perceptual brightness measure.

$$X = \int_{380\,\mathrm{nm}}^{800\,\mathrm{nm}} I(\lambda)\,\overline{x}(\lambda)\,d\lambda \tag{2}$$

$$Y = \int_{380\,\mathrm{nm}}^{800\,\mathrm{nm}} I(\lambda)\,\overline{y}(\lambda)\,d\lambda \tag{3}$$

$$Z = \int_{380\,\mathrm{nm}}^{800\,\mathrm{nm}} I(\lambda)\,\overline{z}(\lambda)\,d\lambda \tag{4}$$

https://doi.org/10.5194/egusphere-2026-3347
Preprint. Discussion started: 11 August 2026

The next step is to convert the CIE XYZ tristimulus values of the simulated spectrum to standard RGB (sRGB) to obtain the corresponding colour.

The sRGB images discussed below represent the corresponding visual impression of an observer on the Earth's surface. Therefore, the luminance of each individual pixel has been preserved and varies according to the position of the Sun and the viewing geometry. The simulated radiance values span several orders of magnitude in luminance, which exceeds the dynamic range of standard display devices and would render large portions of each image as either completely black or completely white. To compress this dynamic range while preserving perceptual colour relationships, the Reinhard tone mapping operator (Reinhard et al., 2002) was applied to the luminance Y:

$$Y' = Y/(1+Y) \tag{5}$$

This operator maps the unbounded luminance range to the displayable range. The chromaticity is preserved by scaling X and Z proportionally to the mapped luminance:

$$X' = X \cdot (Y'/Y), \quad Z' = Z \cdot (Y'/Y) \tag{6}$$

The mapped XYZ values were then converted sRGB.

Since the absolute luminance decreases by approximately one order of magnitude per 2° increase in SZA (see Fig. A3), a global normalisation would render images for high SZAs essentially black. The Reinhard operator is therefore applied to control intra-image contrast by compressing the dynamic range within each SZA scene. Each image is then normalised to its own maximum sRGB value over all pixels and colour channels (R, G, B) to maximise the visible colour information at each SZA independently:

$$\mathrm{sRGB}_{\mathrm{display}} = \mathrm{sRGB}/\max(\mathrm{sRGB}) \cdot 255 \tag{7}$$

The sRGB results are presented in the following section.

Since the colours displayed may vary depending on the output device, the CIE chromaticity coordinates x, y, which represent colours independently of brightness, were also calculated:

$$x = \frac{X}{X+Y+Z} \qquad y = \frac{Y}{X+Y+Z}. \tag{8}$$

The chromaticity coordinates enable an objective representation of colours in the so-called 2-D CIE x, y chromaticity diagram (see Fig. 1). The arc of the CIE chromaticity diagram is formed by the pure spectral colours, i.e. monochromatic light of a single wavelength, with the corresponding wavelengths. The connecting line ("line of purples") at the bottom of the arc are the non-spectral colours, i.e. colours whose hues are not produced by a single wavelength in the visible spectrum. The cross "x" in the CIE chromaticity diagram represents the chromaticity values for the white point, i.e. the colour perception of white. The CIE chromaticity diagram enables the objective representation of colours, here only the position within the diagram is objective. This representation is also used in the present study.

https://doi.org/10.5194/egusphere-2026-3347
Preprint. Discussion started: 11 August 2026

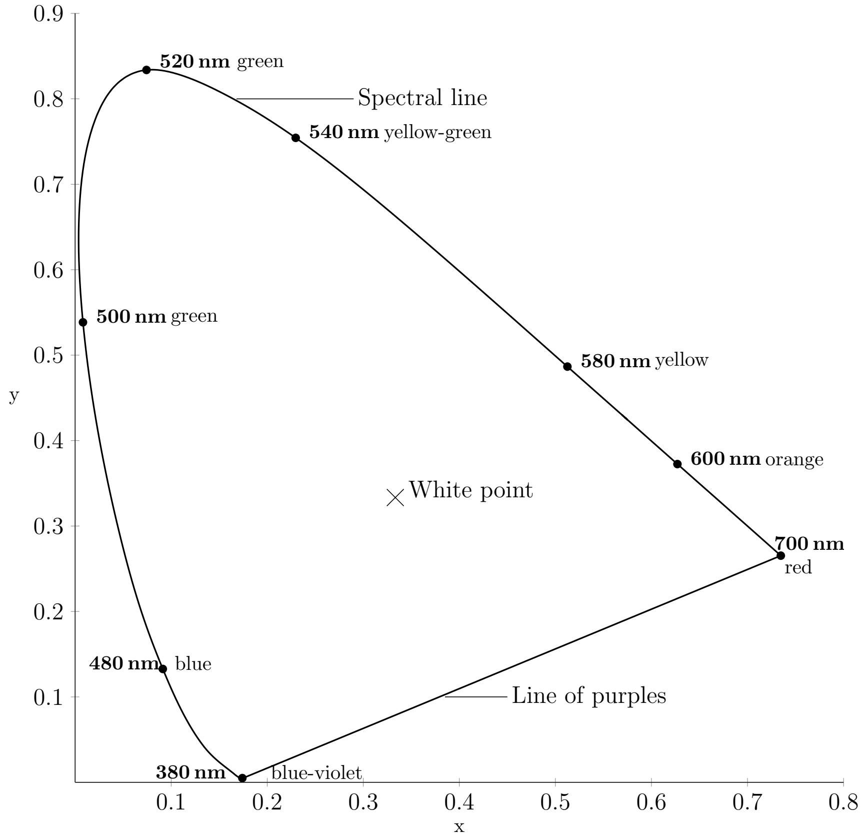

Figure 1. Schematic representation of the CIE chromaticity diagram.

3 Results and discussion

Figure 2 shows the simulated colours (sRGB) for an observer on the Earth's surface with SZA = 90°, 15° N latitude and different SAI scenarios (see Tab. 1): Volc10Tg + SAI_nhoff, month 1 (a) and 5 (b), Volc10Tg + SAI_off month 1 (c) and 5 (d), and Volc50Tg + SAI_off, month 1 (e) and 5 (f). All panels show the red-orange colouring of the horizon (VZA = 90°) toward the Sun (SAA $\approx\leq$ 30°), as well as a whitish-greenish area for small SAAs, which is surrounded by an orange-yellow ring and the blue sky. At first glance, there appear to be no differences between the scenarios in the first month (left column), however, the whitish maximum in panel c has a less concentrated and slightly more diffuse structure and the orange-yellow ring appears smaller. The close visual similarity of the scenarios in the first month is consistent with the findings of Quaglia et al. (2024), which show that after the eruption, global burden and SAOD (about 0.15) remain nearly similar for the scenarios. The ring-like structure becomes more clearly visible in the fifth month of the Volc50Tg + SAI_off scenario, when the maxima in global sulphate burden and SAOD (about 0.6) are reached (see Fig. 1 in Quaglia et al. (2024)).

https://doi.org/10.5194/egusphere-2026-3347
Preprint. Discussion started: 11 August 2026

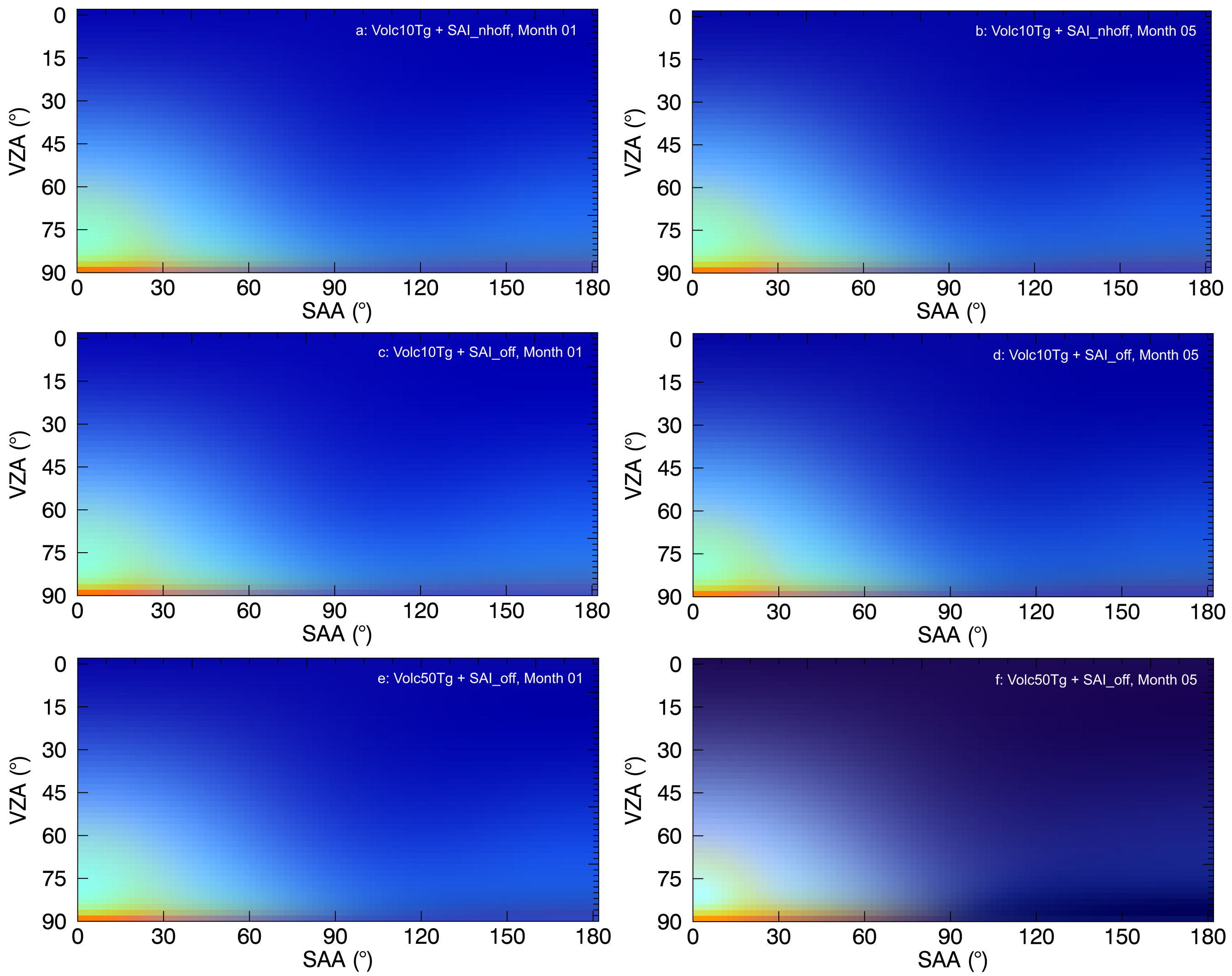

Figure 2. Simulated colours for an observer on the Earth's surface with SZA = 90°. a: Volc10Tg + SAI_nhoff, month 1, b: Volc10Tg + SAI_nhoff, month 5, c: Volc10Tg + SAI_off, month 1, d: Volc10Tg + SAI_off, month 5, e: Volc50Tg + SAI_off, month 1, and f: Volc50Tg + SAI_off, month 5. All panels for 15° N latitude.

The results in panel f of Fig. 2 show, besides the generally reduced brightness, an orange-reddish horizon on the solar side, as well as a clearly defined ring structure between SAA 0 – 30° and VZA 75 – 85°. In addition, a distinct whitish-greenish brightness maximum is visible at VZA ≈ 75 — 85°. This whitish maximum is surrounded by a ring that gradually turns orange toward the outside. On the zenith side of this maximum, at VZA ≈ 60°, the sky becomes darker and bluer again.

The combination of a localised brightness enhancement, surrounded by a darker annular region on the zenith side, is characteristic of a Bishop's Ring, i.e. an optical phenomenon caused by forward Mie scattering of sunlight on stratospheric aerosol

https://doi.org/10.5194/egusphere-2026-3347
Preprint. Discussion started: 11 August 2026

particles. However, it must first be verified whether the simulations actually depict a Bishop's Ring, or merely the Sun's aureole, which becomes progressively brighter toward the Sun.

For this, the left panel of Fig. 3 shows the luminance (Y) as a function of VZA (°) for panel f of Fig. 2 and SAA = 0°. The luminance depicts a distinct local maximum at VZA ≈ 82°, after which it decreases until VZA = 90°. To further support this observation, the red-to-blue ratio (R/B ratio) was examined to determine whether the maximum is wavelength-dependent (blue being further out than red). The right panel of Fig. 3 visualises the corresponding R/B ratio as a function of VZA (°) and SAA = 0°. The graph shows a small local maximum at VZA ≈ 70° (R/B ≈ 1.8), followed by a minimum at VZA ≈ 82° and a sharp rise from VZA ≈ 85°. This supports the hypothesis of the Bishop's Ring signature, with increased red dominance in the ring. The sharp rise from VZA ≈ 85° is due to Rayleigh scattering, which causes the horizon to turn reddish at sunset. Furthermore, Fig. 3 highlights that the Y maximum (at VZA ≈ 82°) and the R/B ratio maximum (at VZA ≈ 70°) do not occur at the same position. At VZA ≈ 70°, red is dominant, which means there is an outer reddish ring. In contrast, at VZA ≈ 82°, the overall brightness is at its maximum, i.e. there is a whitish-bright core. This corresponds exactly to the classic Bishop's Ring structure.

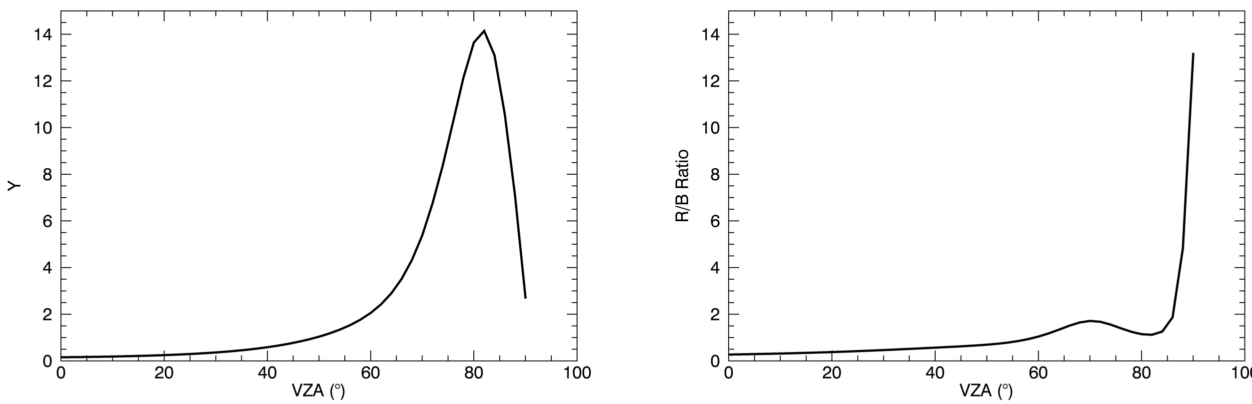

Figure 3. Left panel: Luminance (Y) as a function of VZA (°) for panel f of Fig. 2 and SAA = 0°. Right panel: R/B ratio as function of VZA (°) for panel f of Fig. 2 and SAA = 0°.

The same conclusion can also be drawn for the other scenarios shown in Fig. 2, although the maxima of the respective functions are not as pronounced (not shown). The simulation results also show that the Bishop's rings are much more pronounced in the fifth month (right column of Fig. 2) and that the coloured rings appear more orange. However, the most significant change is observed in the Volc50Tg + SAI_off case (panel f of Fig. 2). It can be concluded that, for the scenarios examined here, a Bishop's Ring is very likely to be observed when the Sun is on the horizon. This is particularly pronounced in the fifth month of the Volc50Tg + SAI_off scenario, when the global sulphate burden and the global SAOD (about 0.6, see Fig. 1 in Quaglia et

https://doi.org/10.5194/egusphere-2026-3347
Preprint. Discussion started: 11 August 2026

al. (2024)) reach their maximum values. Furthermore, the Bishop's Ring phenomenon does not occur in the case of SAI only (without a volcanic eruption) in the studies carried out here (see Fig. A4).

The decrease in brightness with increasing SZA and aerosol load can be demonstrated consistently and quantitatively in the course of the luminance Y. Figure 4 shows the probability distributions of the luminance Y for SZAs of 90, 92, 94, 96, and 98°, as histograms of $\log_{10}(Y)$ over all viewing directions (VZAs = 0 — 90°, 2° steps, and SAAs = 0 — 180°, 2° steps), calculated with 50 equally spaced bins over the full luminance range. The upper panel illustrates the probability distributions of Y for the first month of the Volc10Tg + SAI_off scenario and the lower panel for the first month of the Volc50Tg + SAI_off scenario - both for 15° N latitude. Consistent with the simulated colours shown before, the Volc10Tg + SAI_off case (upper panel) shows higher Y values than the Volc50Tg + SAI_off case (lower panel). The top panel shows narrow, almost symmetrical distributions with peaks in the range from approximately -5 to -1. As the SZA increases, the peak shifts significantly to the left (towards lower Y values), as expected. This means the scene becomes darker. In contrast, the lower panel shows broad and asymmetric distributions. In particular, at SZA = 98° (purple line), a bimodal structure (two peaks) can be observed. The broader and antisymmetric structure can likely be attributed to the larger stratospheric aerosol load, which leads to greater variability in brightness across viewing directions depending on the SAA, i.e. between the solar and anti-solar horizon. Overall, the peaks are shifted further to the left (lower Y values), which means that the scene is darker. Furthermore, the curves are less sharply defined and have longer tails, suggesting greater spatial variability in brightness. The Volc50Tg + SAI_off scenario thus results in a much stronger attenuation of light, a wider spread of brightness values and more complex distribution patterns than the Volc10Tg + SAI_off scenario.

The qualitative change in brightness as the SZA increases, and the resulting colours for the first (left column) and fifth (right column) month of the Volc10Tg + SAI_off scenario, are shown in Fig. 5. For the Sun on the horizon (SZA = 90°), the Bishop's Ring structure discussed above is visible. At SZA of 92°, the Earth's shadow and the Belt of Venus (slightly purple) can be seen on the anti-solar (SAAs $\geq$ 90°) side. Consistent with previous studies, the Belt of Venus appears colour-suppressed, as it requires precisely the right conditions (AOD) to appear in its typical pinkish colours (e.g., Lee, 2015). On the solar side, an orange-red colour can be seen on the horizon, which then changes to a slightly greenish hue above and subsequently to a bluish colour. The greenish colouring above the orange-red horizon is also clearly visible at SZAs of 94° and 96°. For the first month, the coarse mode sulphate aerosol particles exhibit median radii of $\approx$ 500 nm at 20 – 22 km altitude and median radii between 600 and 700 nm at altitudes of 19 – 15 km. The scattering cross-section of the coarse mode exceeds that of the accumulation mode by approximately a factor of 75, making it the optically dominant component. As discussed by von Savigny et al. (2024), for the median radii of the particles between $\approx$ 500 and 700 nm, the scattering cross-section in the visible spectral range increases with wavelength, which results in the so-called anomalous scattering. In this case, the particles scatter the red component of the transmitted sunlight stronger than the blue component, so that the light perceived by an observer on the Earth's surface appears greenish.

https://doi.org/10.5194/egusphere-2026-3347
Preprint. Discussion started: 11 August 2026

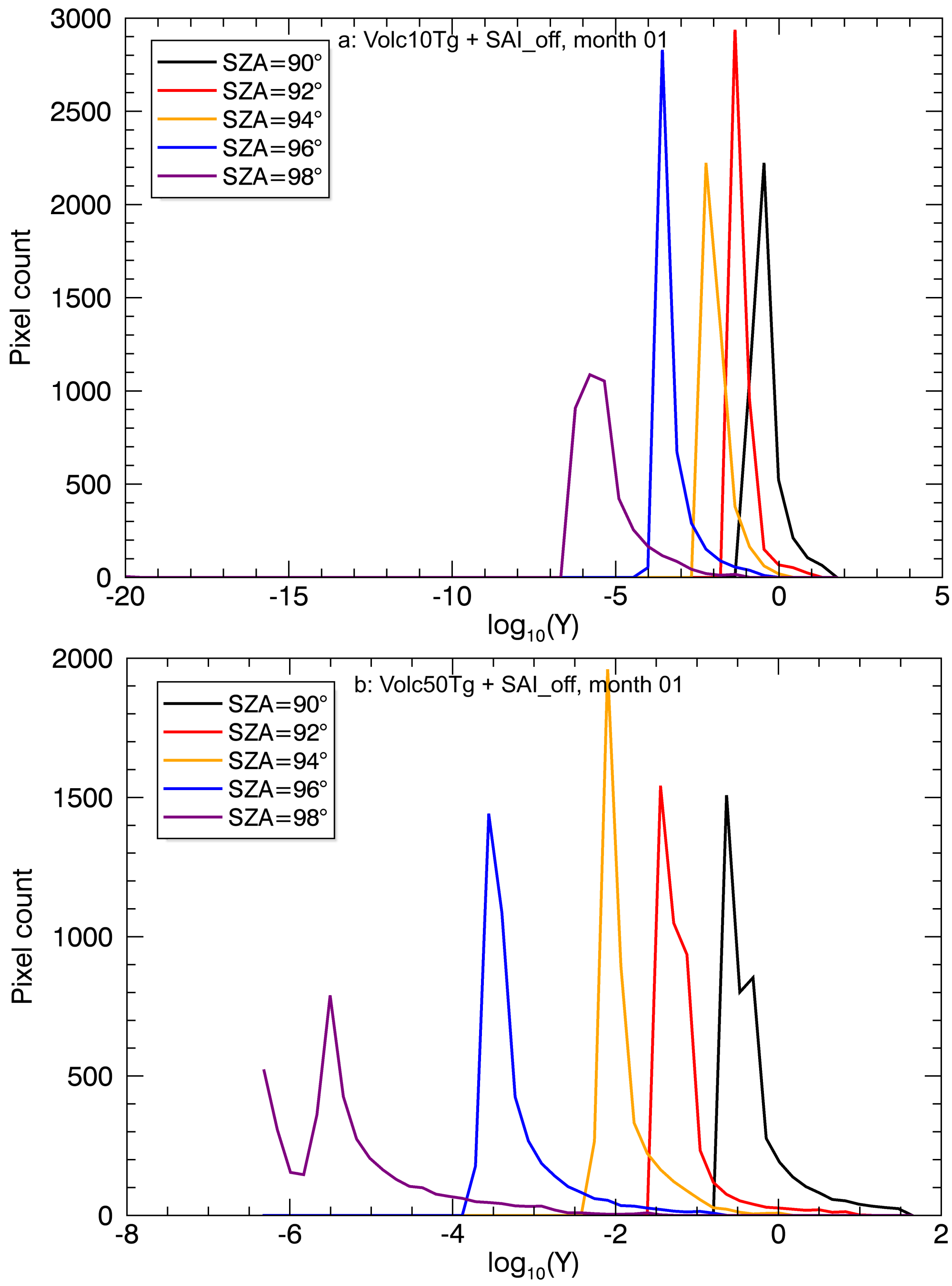

Figure 4. Probability distributions of the CIE luminance Y for SZAs of 90, 92, 94, 96, and 98°, shown as histograms of $\log_{10}(Y)$ over all viewing directions (VZAs = 0 — 90°, 2° steps, and SAAs = 0 — 180°, 2° steps), calculated with 50 equally spaced bins over the full luminance range. Each distribution represents 4186 pixels. Upper panel: First month of the Volc10Tg + SAI_off scenario. Lower panel: First month of the Volc50Tg + SAI_off scenario. Both for 15° N latitude.

https://doi.org/10.5194/egusphere-2026-3347
Preprint. Discussion started: 11 August 2026

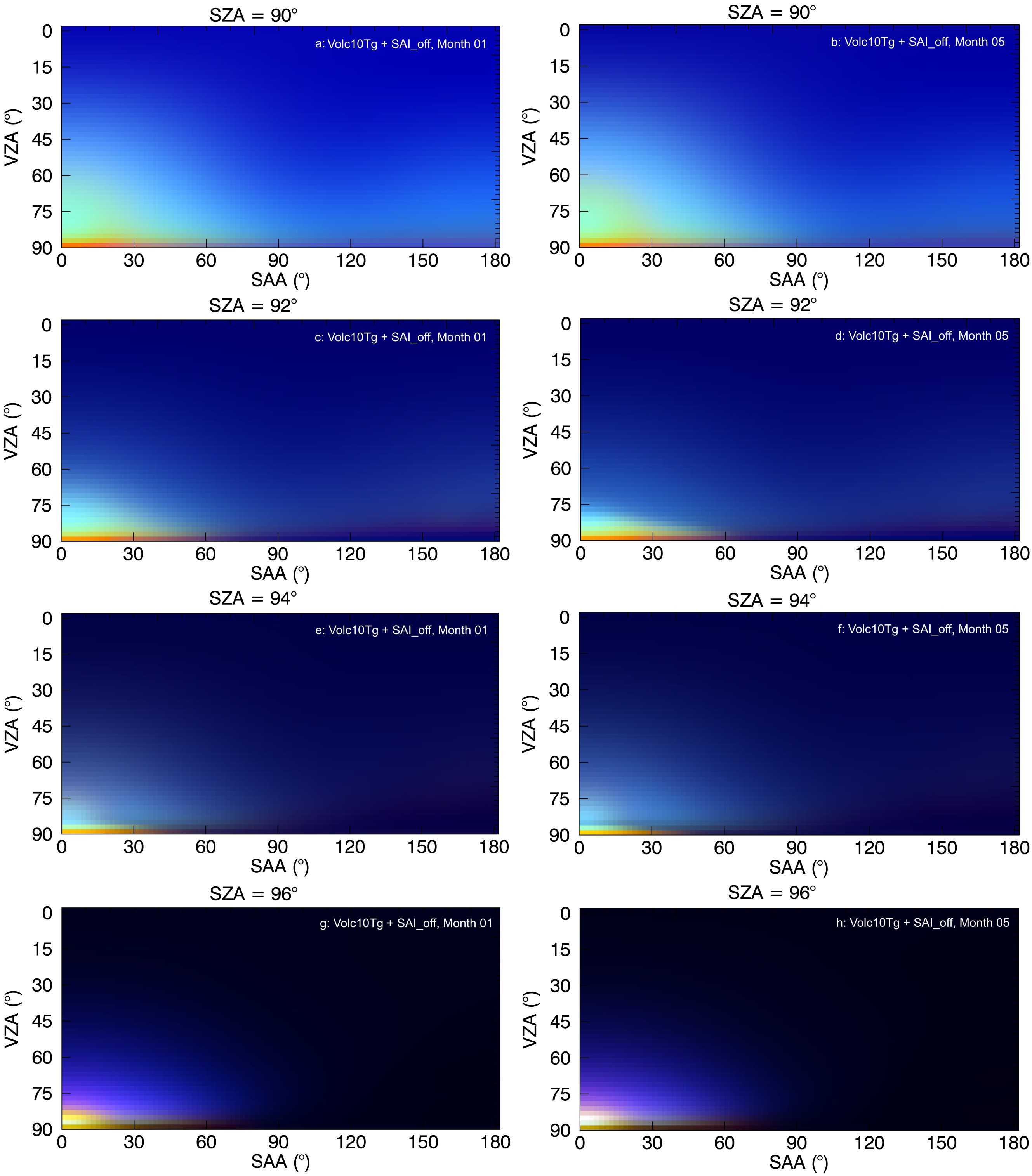

Figure 5. Simulated colours for an observer on the Earth's surface with SZAs = 90 – 96°, 15° N latitude and for the first (left column) and fifth (right column) month of the Volc10Tg + SAI_off scenario.

https://doi.org/10.5194/egusphere-2026-3347
Preprint. Discussion started: 11 August 2026

For SZA = 96°, another phenomenon can be observed alongside the greenish colour: purple light. The purple colour is consistent with the purple light phenomenon described by e.g. Lee and Hernández-Andrés (2003). The phenomenon requires reddened sunlight transmitted through the lower atmosphere combined with blue Rayleigh-scattered light from higher layers (Lee and Hernández-Andrés, 2003). These findings for SZA = 96° also support the conclusion that increased stratospheric aerosol loading is associated with pronounced purple colours of the twilight sky. Similar conclusions can be drawn for the fifth month of the scenario, although the purple and green colours appear more distinct (panel f and h).

The results show that, in the first month of the Volc10Tg + SAI_off scenario, alongside the Bishop Ring with the Sun on the horizon, distinct twilight colours appear, with a greenish colouring of the horizon, which is very likely due to anomalous scattering. The green colour on the horizon should not be mistaken with the green band phenomenon, which can also be observed under background conditions at sunset and during the following twilight. The main mechanisms behind this phenomenon are Rayleigh scattering and absorption in the Chappuis bands of stratospheric ozone (Lange et al., 2023). A greenish colouring of the horizon can also be observed in the case of SAI without volcanic disturbance (Fig. A4). With median radii for the coarse mode between about 500 and 700 nm, anomalous scattering is very likely the explanation. Under the SAI-only conditions, the simulations for SZA = 90° (Fig. A4) also exhibit extended reddish colouring near the horizon, including the anti-solar direction. This feature may be related to enhanced multiple scattering and backscattering, producing a qualitatively Belt-of-Venus-like appearance. However, the effect is not similarly pronounced in the SAI cases with volcanic activity, suggesting a potential sensitivity to the corresponding SAOD and phase function. For the SZA of 92° (Fig. A5), the Belt of Venus is clearly visible alongside the Earth's Shadow, which is not the case for the scenario with the volcanic eruption. At higher SZAs, neither greenish colours on the horizon nor the purple light are visible (see Fig. A5). In the present simulations, these phenomena are observed exclusively in the presence of volcanic activity during SAI. It should be emphasized that no general claims are made regarding the exclusivity of these optical phenomena to combined volcanic and SAI scenarios. The focus of the study is solely on how sky colours are modified following a volcanic eruption in a geoengineered world.

The different SAI scenarios (see Tab. 1), which are presented following the volcanic eruption with 10 Tg of sulphur dioxide injected, raise the question of to what extent these different approaches (Volc10Tg + SAI_nhoff and Volc10Tg + SAI_off) result in different sky colours. The results shown in Fig. 2 indicate that nearly similar colours can be observed for an SZA of 90°. The same conclusion can be drawn for SZA = 92° (Fig. 6). These results, here for 15° N latitude, can be explained by the global and zonal sulphate burden and SAOD. For month 1 and month 5 (when both global sulphate burden and SAOD reach their maximum (both about 0.24, see Fig. 1 in Quaglia et al. (2024))), the respective values for Volc10Tg + SAI_nhoff and Volc10Tg + SAI_off are nearly similar, which explains the almost identical colour impressions (see Fig. 1 in Quaglia et al. (2024)). The simulations for SZA = 94° (Fig. 7) and 96° (Fig. 8) support these conclusions. Although minor variations in colour can be observed, there are no significant changes in the perceived colours within the two scenarios.

https://doi.org/10.5194/egusphere-2026-3347
Preprint. Discussion started: 11 August 2026

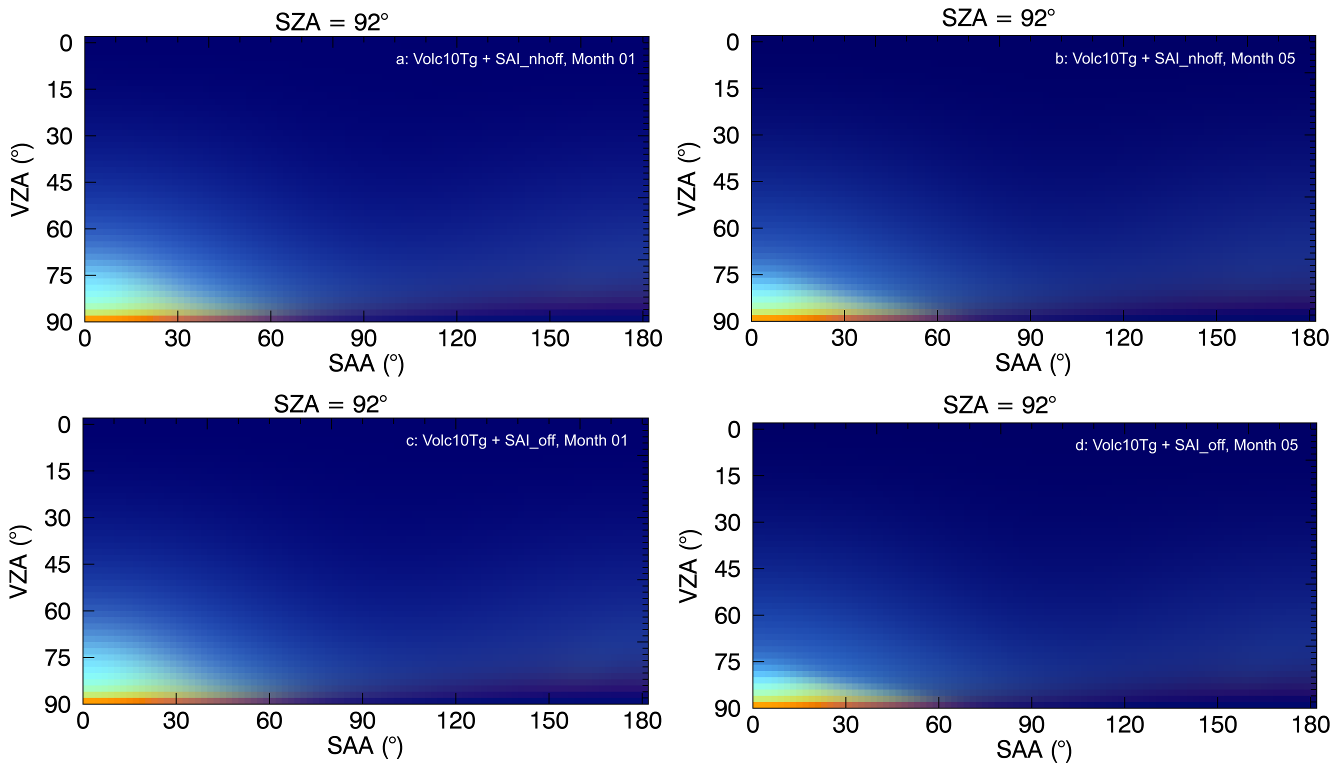

Figure 6. Simulated colours for an observer on the Earth's surface with SZA = 92°. Upper row: Month 1 and 5 for the Volc10Tg + SAI_nhoff scenario. Lower row: Month 1 and 5 for the Volc10Tg + SAI_off scenario. All panels for 15° N latitude.

https://doi.org/10.5194/egusphere-2026-3347
Preprint. Discussion started: 11 August 2026

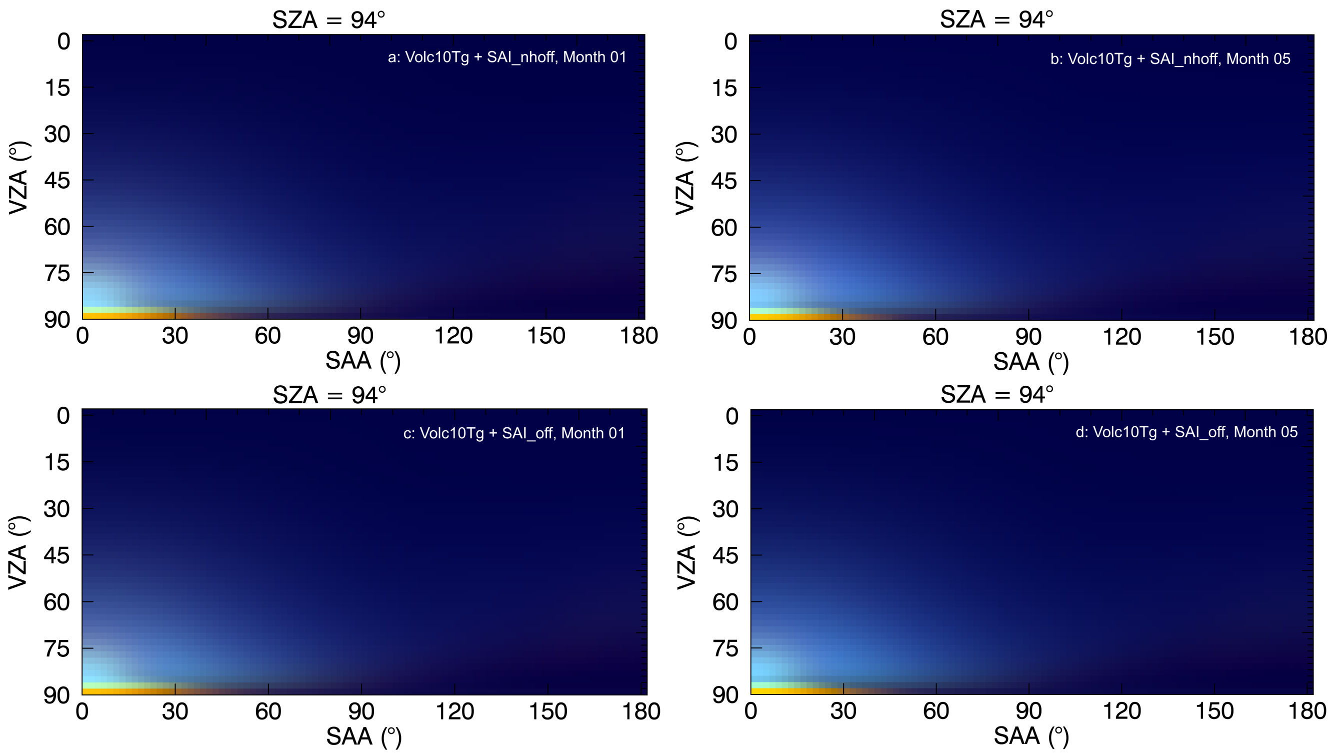

Figure 7. Same as Fig. 6 but for SZA = 94°.

https://doi.org/10.5194/egusphere-2026-3347
Preprint. Discussion started: 11 August 2026

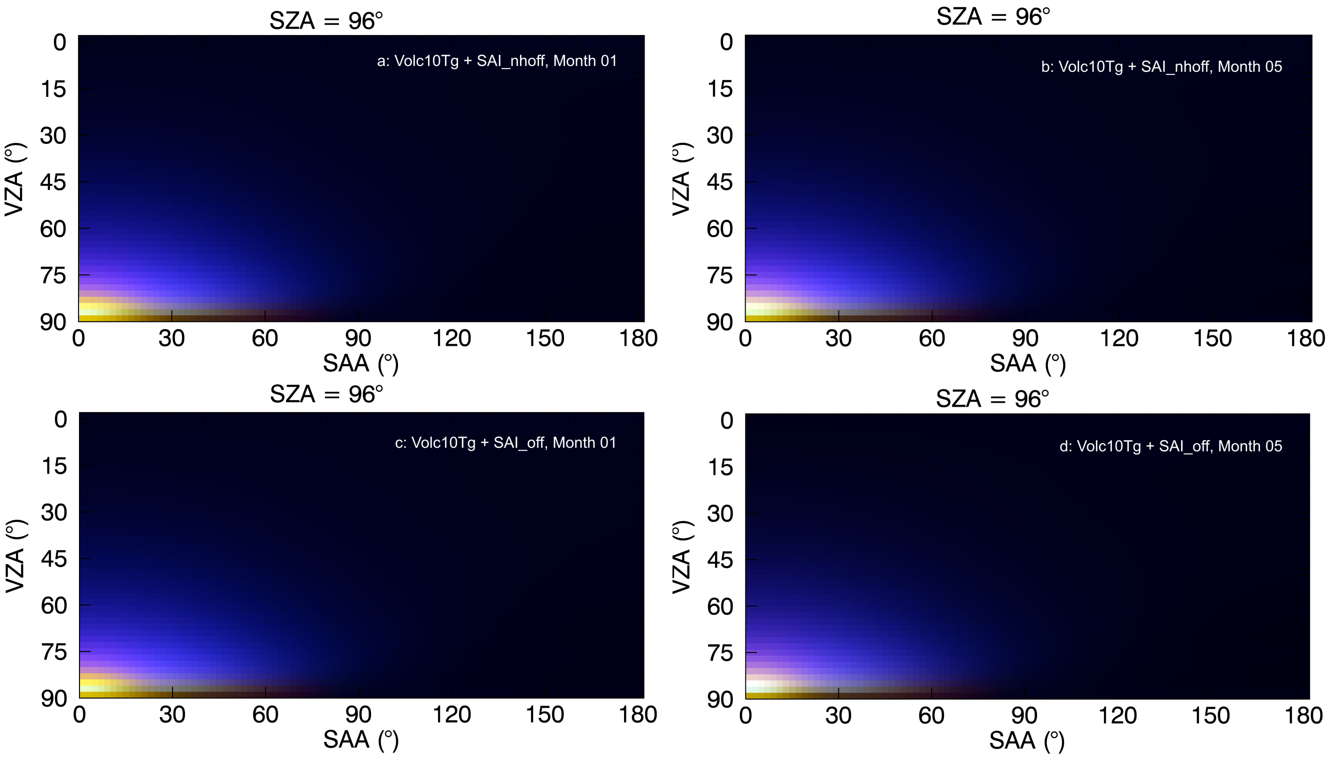

Figure 8. Same as Fig. 6 but for SZA = 96°.

The simulation results show that, in a geoengineered world with volcanic eruptions various optical phenomena are to be expected, considering the SAI emission rates, scenarios and months examined here. These include Bishop's Rings, unusual green twilight colours, purple lights and intense twilight colours, as well as suppressed colours of the Belt of Venus, depending on the magnitude of the volcanic eruption and the month analysed. It should be noted, however, that the colours shown above may vary depending on the output medium. One way of representing colours objectively is the CIE colour system (see Sect. 2.3). Figure A6 in the appendix therefore shows CIE chromaticity diagrams corresponding to Fig. 5 (left column), which incorporate all the key optical phenomena discussed here. Each curve corresponds to a fixed SAA, with points along each curve representing VZAs from VZA = 0° (zenith) to VZA = 90° (horizon). More details are given in Sect. 2.3.

4 Conclusions

By using CESM2(WACCM6) model simulations, radiative transfer simulations with SCIATRAN and subsequent colour modelling, this study has demonstrated what sky colours can probably be expected in a geoengineered world following a volcanic eruption. The study thus bridges a gap between existing research, which has previously examined sky colours following vol-

https://doi.org/10.5194/egusphere-2026-3347
Preprint. Discussion started: 11 August 2026

canic eruptions and SAI separately. While focusing on the effects of volcanic eruptions in a geoengineered world, the study does not imply that the resulting optical phenomena are exclusive to such scenarios.

Furthermore, this study investigated whether different SAI scenarios initiated following the volcanic eruption with 10 Tg sulphur dioxide result in different colour phenomena. In addition to changes in brightness, various optical phenomena could be identified. Bishop's Rings when the Sun is on the horizon, which occur more intensively in the fifth month of the Volc50Tg + SAI_off scenario. Furthermore, unusual greenish colouring of the horizon during twilight is seen, which is very likely due to anomalous scattering. In addition, intense purple light was observed, confirming previous studies which concluded that an increased aerosol loading is necessary for the purple colour to appear distinctly. In the present simulations, these optical phenomena occur exclusively in scenarios combining SAI and volcanic activity, under the cases and conditions analysed here. An exception is the greenish colouring of the horizon at SZAs of 90 and 92°, which can also occur in the analysed SAI-only conditions. Furthermore, it has been shown that, taking into account the conditions and scenarios examined here, no significant differences in sky colour are to be expected across different SAI scenarios after the volcanic eruption with 10 Tg sulphur dioxide and 15° N latitude.

Code and data availability. The radiative transfer model SCIATRAN can be downloaded via: https://www.iup.uni-bremen.de/sciatran/.

Appendix A

https://doi.org/10.5194/egusphere-2026-3347
Preprint. Discussion started: 11 August 2026

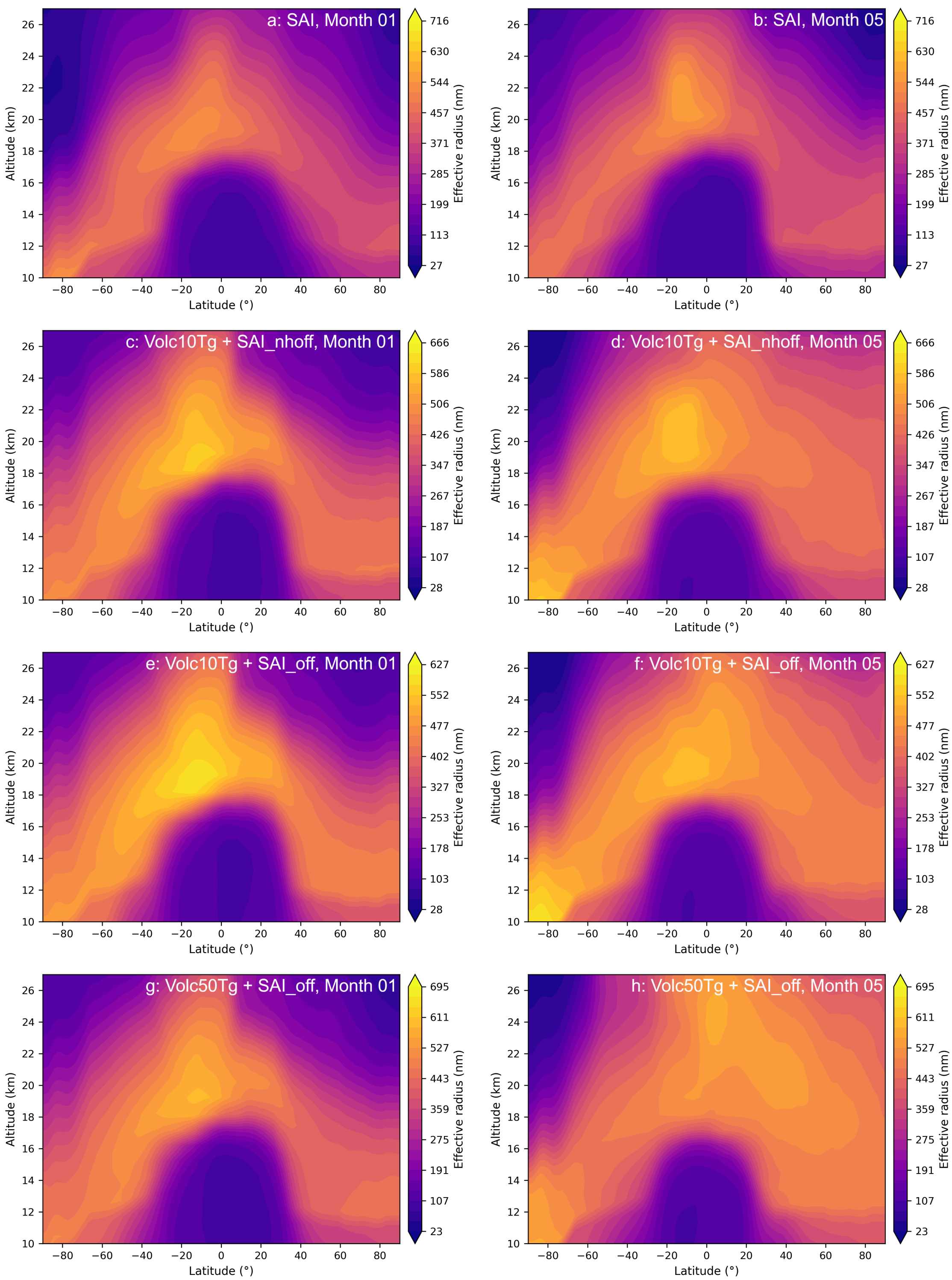

Figure A1. Effective radius for the different scenarios (see Tab. 1) for month 1 (left column) and 5 (right column) based on the CESM2(WACCM6) model simulations.

https://doi.org/10.5194/egusphere-2026-3347
Preprint. Discussion started: 11 August 2026

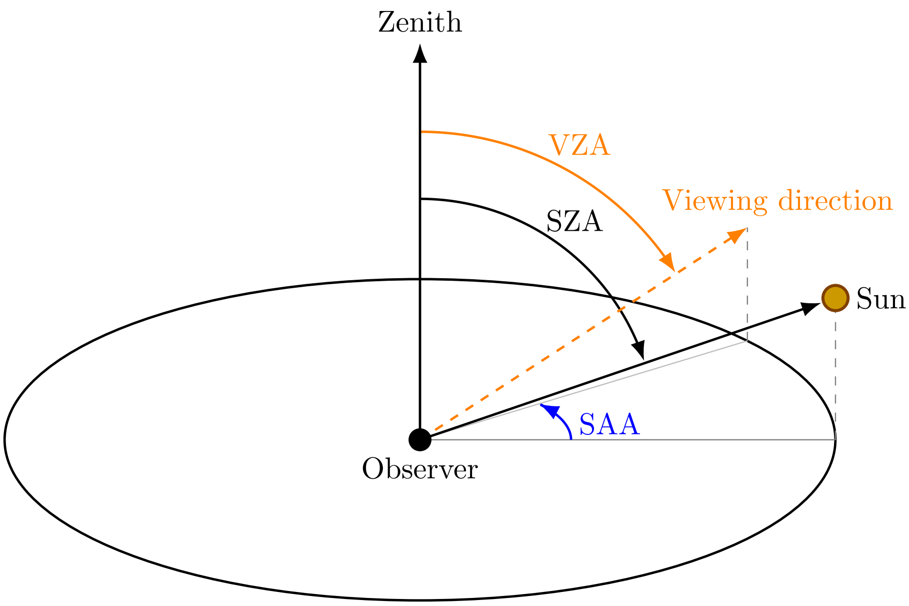

Figure A2. Definition of the viewing geometry in SCIATRAN with VZA as viewing zenith angle, SZA as solar zenith angle, and SAA as solar azimuth angle.

https://doi.org/10.5194/egusphere-2026-3347
Preprint. Discussion started: 11 August 2026

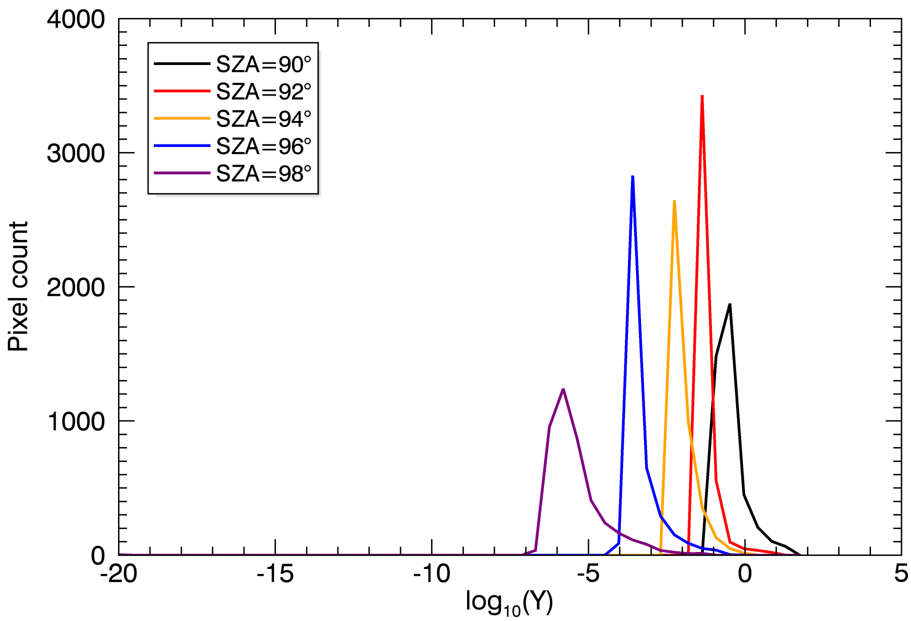

Figure A3. Probability distributions of the CIE luminance Y for SZAs of 90, 92, 94, 96, and 98° and scenario 2 (see Tab. 1), shown as histograms of $\log_{10}(Y)$ over all viewing directions (VZAs = 0 — 90°, 2° steps, and SAAs = 0 — 180°, 2° steps), calculated with 50 equally spaced bins over the full luminance range. Each distribution represents 4186 pixels. The distributions shift by approximately one order of magnitude per 2° increase in SZA.

https://doi.org/10.5194/egusphere-2026-3347
Preprint. Discussion started: 11 August 2026

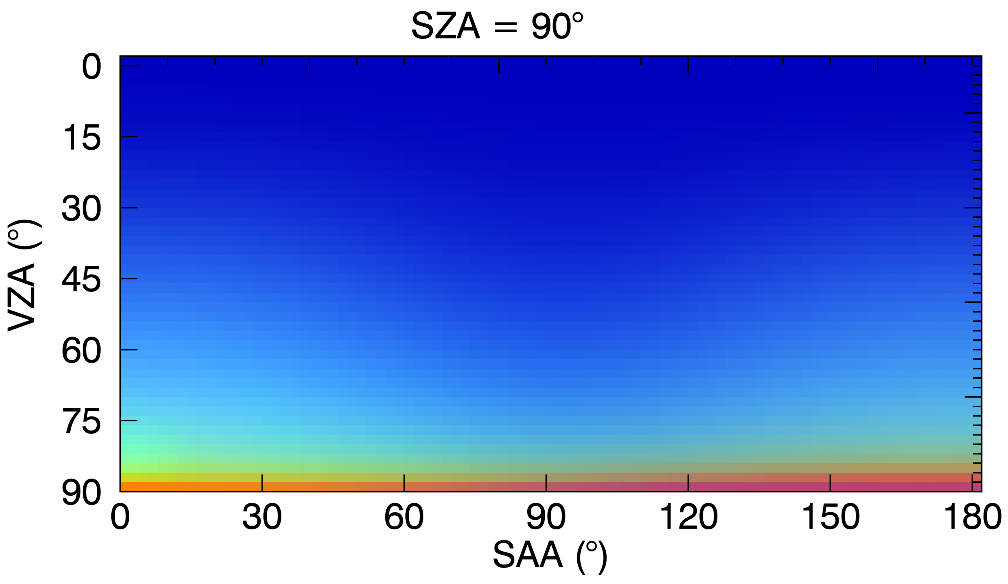

Figure A4. Simulated colours for an observer on the Earth's surface with SZA = 90°, 15° N latitude and the first month of the SAI scenario without volcanic eruption.

https://doi.org/10.5194/egusphere-2026-3347
Preprint. Discussion started: 11 August 2026

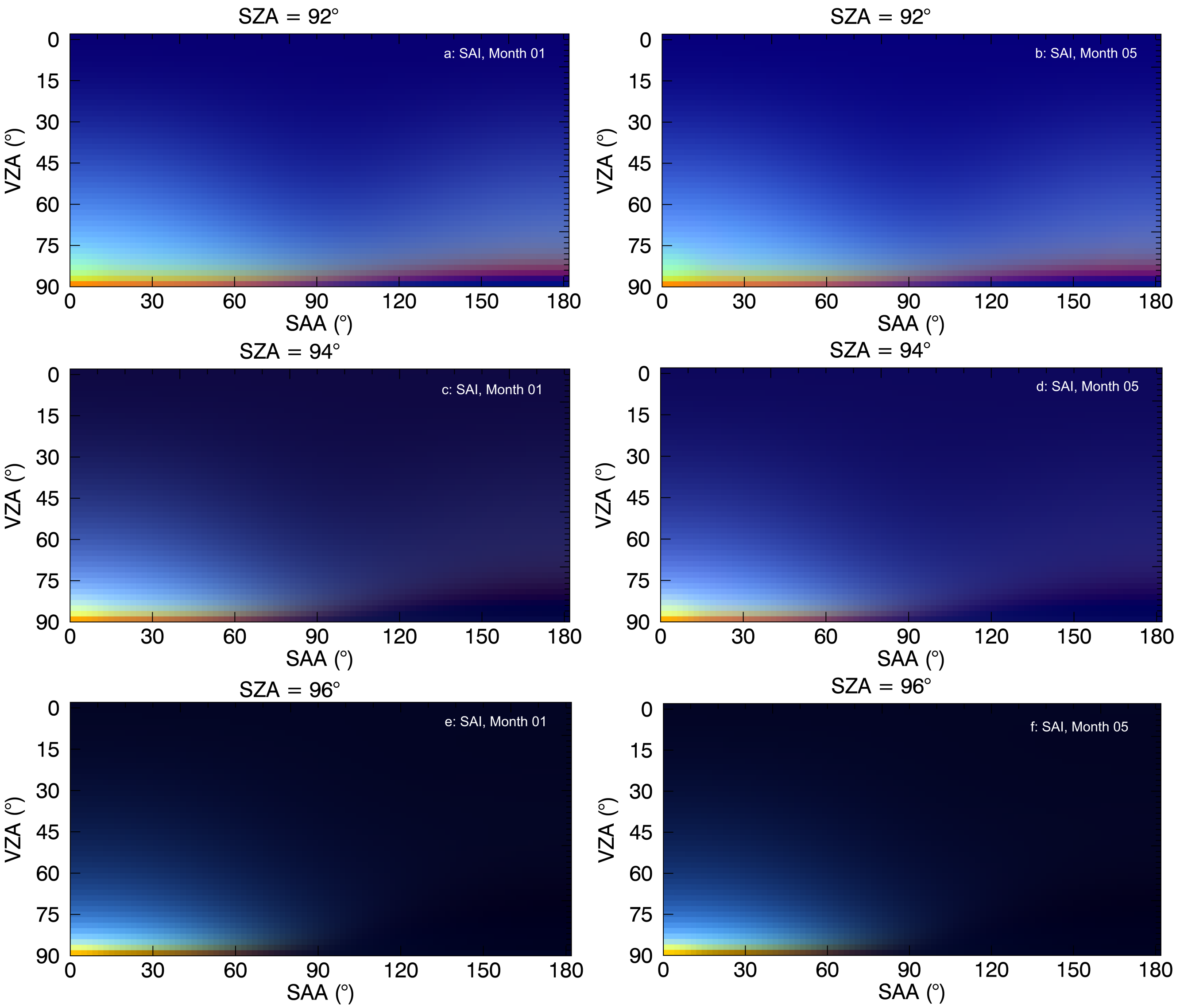

Figure A5. Simulated colours for an observer on the Earth's surface with SZA = 92 – 96°, 15° N latitude and the first (left column) and fifth (right column) month of the SAI scenario without volcanic eruption.

https://doi.org/10.5194/egusphere-2026-3347
Preprint. Discussion started: 11 August 2026

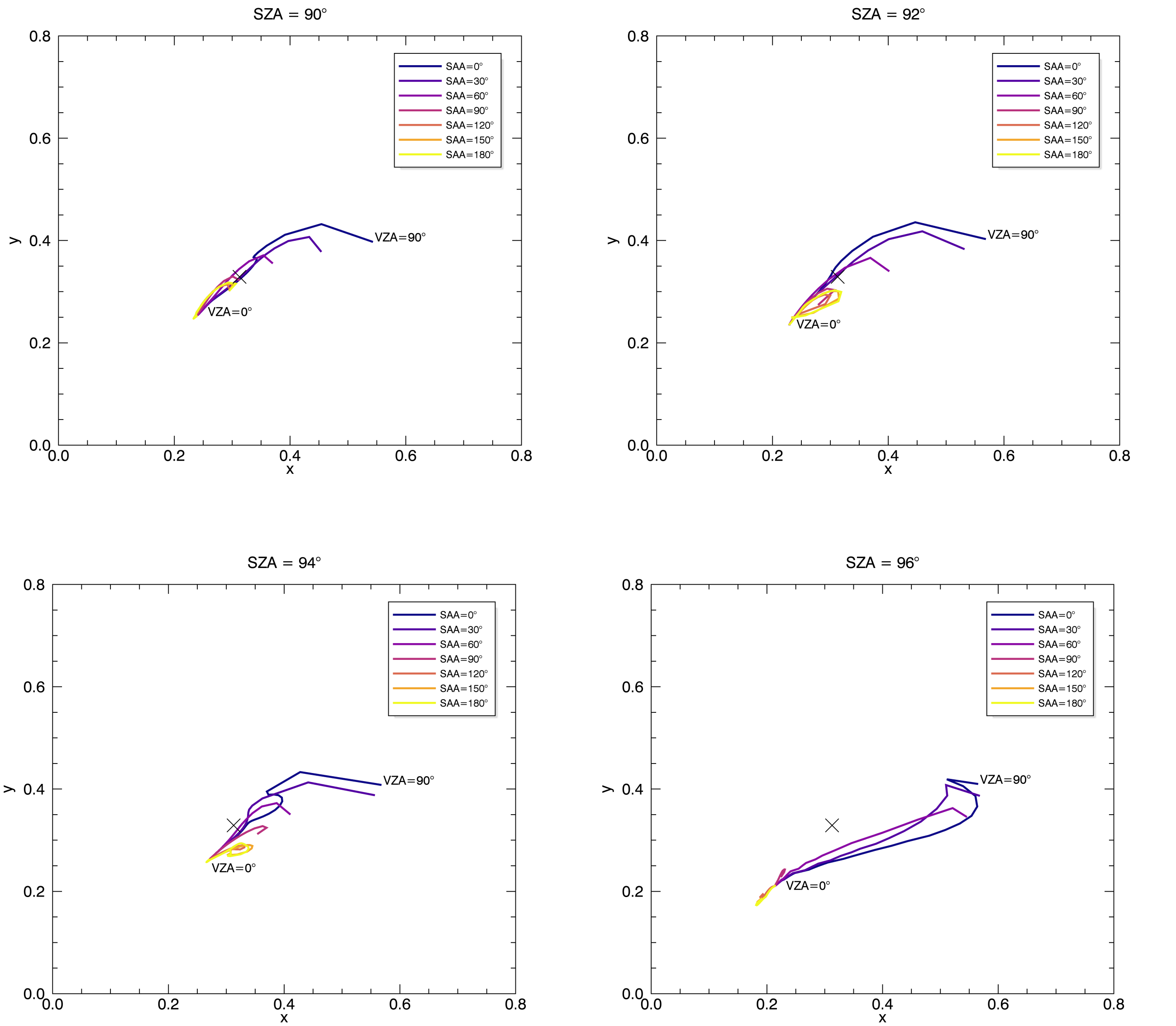

Figure A6. CIE chromaticity diagrams corresponding to Fig. 5 (left column). VZA = 0° indicates the start point (zenith) and VZA = 90° the end point (horizon), with the loop forming as the colour trajectory reverses direction near the horizon.

Author contributions. AL outlined the project. AL performed the radiative transfer simulations, the colour modelling calculations, and wrote the first version of the manuscript. IQ and DV carried out the CESM2(WACCM6) model runs. All authors reviewed and edited the manuscript.

https://doi.org/10.5194/egusphere-2026-3347
Preprint. Discussion started: 11 August 2026

Competing interests. The authors declare that they have no competing interests.

Acknowledgements. We are indebted to the Institute of Environmental Physics at the University of Bremen for the access to the SCIATRAN radiative transfer model.

References

Budyko, M. I.: Climatic changes, American Geophysical Society, Washington, D.C., doi:10.1029/SP010, 1977.

Commission Internationale De L'Eclairage (CIE): CIE 15: 2004 – Colorimetry 3rd edn., Technical Report, ISBN 3901906339, 2004.

Crutzen, P. J.: Albedo enhancement by stratospheric sulfur injections: A contribution to resolve a policy dilemma?, Climatic Change, 77, 211–219, 2006.

Danabasoglu, G., Lamarque, J.-F., Bacmeister, J., Bailey, D. A., DuVivier, A. K., Edwards, J., Emmons, L. K., Fasullo, J., Garcia, R., Gettelman, A., Hannay, C., Holland, M. M., Large, W. G., Lauritzen, P. H., Lawrence, D. M., Lenaerts, J. T. M., Lindsay, K., Lipscomb, W. H., Mills, M. J., Neale, R., Oleson, K. W., Otto-Bliesner, B., Phillips, A. S., Sacks, W., Tilmes, S., van Kampenhout, L., Vertenstein, M., Bertini, A., Dennis, J., Deser, C., Fischer, C., Fox-Kemper, B., Kay, J. E., Kinnison, D., Kushner, P. J., Larson, V. E., Long, M. C., Mickelson, S., Moore, J. K., Nienhouse, E., Polvani, L., Rasch, P. J., and Strand, W. G.: The Community Earth System Model Version 2 (CESM2), J. Adv. Model. Earth Sy., 12, e2019MS001916, https://doi.org/10.1029/2019MS001916, 2020.

Davis, N. A., Visioni, D., Garcia, R. R., Kinnison, D. E., Marsh, D. R., Mills, M. J., Richter, J. H., Tilmes, S., Bardeen, C., Gettelman, A., Glanville, A. A., MacMartin, D. G., Smith, A. K., and Vitt, F.: Climate, variability, and climate sensitivity of "Middle Atmosphere" chemistry configurations of the Community Earth System Model Version 2, Whole Atmosphere Community Climate Model Version 6 (CESM2(WACCM6)), J. Adv. Model. Earth Sy., 15, e2022MS003579, https://doi.org/10.1029/2022MS003579, 2023.

Eastham, S. D., Butler, A. H., Doherty, S. J., Gasparini, B., Tilmes, S., Bednarz, E. M., Burkhardt, U., Chiodo, G., Cziczo, D. J., Diamond, M.S., Keith, D. W., Leisner, T., MacMartin, D. G., Quaas, J., Rasch, P. J., Sourdeval, O., Steinke, I., Thompson, C., Visioni, D., Wood, R., Xia, L., and Yu,P.: Key Gaps in Models' Physical Representation of Climate Intervention and Its Impacts, Journal of Advances in Modeling Earth Systems, 17, e2024MS004872, https://doi.org/10.1029/2024MS004872, e2024MS004872 2024MS004872, 2025.

Gettelman, A., Hannay, C., Bacmeister, J. T., Neale, R. B., Pendergrass, A. G., Danabasoglu, G., Lamarque, J.-F., Fasullo, J. T., Bailey, D. A., Lawrence, D. M., and Mills, M. J.: High Climate Sensitivity in the Community Earth System Model Version 2 (CESM2), Geophys. Res. Lett., 46, 8329–8337, https://doi.org/10.1029/2019GL083978, 2019.

Kravitz, B., MacMartin, D. G., and Caldeira, K.: Geoengineering: Whiter skies?, Geophys. Res. Lett., 39, L11801, doi:10.1029/2012GL051652, 2012.

Haywood, J. M., Boucher, O., Lennard, C., Storelvmo, T., Tilmes, S., and Visioni, D.: World Climate Research Programme lighthouse activity: an assessment of major research gaps in solar radiation modification research. Frontiers in Climate, 7, 1507479, 2025.

Kravitz, B., MacMartin, D. G., Wang, H., and Rasch, P. J.: Geoengineering as a design problem, Earth Syst. Dynam., 7, 469–497, https://doi.org/10.5194/esd-7-469-2016, 2016.

Lange, A., Baumgarten, G., Rozanov, A., and von Savigny, C.: On the colour of noctilucent clouds, Ann. Geophys., 40, 407–419, https://doi.org/10.5194/angeo-40-407-2022, 2022.

Lange, A., Rozanov, A., and von Savigny, C.: On the twilight phenomenon of the green band, Appl. Opt., 62, 162–171, 2023.

LASP (Laboratory for Atmospheric and Space Physics): SORCE Solar Spectral Irradiance, Spectrum, LASP Interactive Solar Irradiance Data Center (LISIRD), University of Colorado, available at: http://lasp.colorado.edu/lisird/data/sorce_ssi_l3/, (last access: 02.03.2026), 2003.

Lee, R. L., and Hernández-Andrés, J.: Measuring and modeling twilight's purple light, Appl. Opt., 42, 445–457, 2003.

Lee, R. L.: Measuring and modeling twilight's Belt of Venus, Appl. Opt. 54, B194-B203, 2015.

https://doi.org/10.5194/egusphere-2026-3347
Preprint. Discussion started: 11 August 2026

Lemon, A., Keith, D. W., and Albers, S.: Under a not so white sky: visual impacts of stratospheric aerosol injection, Environ. Res. Lett. 20.2, 024060, 2025.

Liu, X., Ma, P.-L., Wang, H., Tilmes, S., Singh, B., Easter, R. C., Ghan, S. J., and Rasch, P. J.: Description and evaluation of a new four-mode version of the Modal Aerosol Module (MAM4) within version 5.3 of the Community Atmosphere Model, Geosci. Model Dev., 9, 505–522, https://doi.org/10.5194/gmd-9-505-2016, 2016.

MacMartin, D. G., Visioni, D., Kravitz, B., Richter, J., Felgenhauer, T., Lee, W. R., Morrow, D. R., Parson, E. A., and Sugiyama, M.: Scenarios for modeling solar radiation modification, P. Natl. Acad. Sci. USA, 119, e2202230119, https://doi.org/10.1073/pnas.2202230119, 2022.

Meinel, A. B., and Meinel, M.: Sunsets, Twilights and Evening Skies, Cambridge University Press, 173 pp., ISBN: 0521406471, 1991.

Meinshausen, M., Nicholls, Z. R. J., Lewis, J., Gidden, M. J., Vogel, E., Freund, M., Beyerle, U., Gessner, C., Nauels, A., Bauer, N., Canadell, J. G., Daniel, J. S., John, A., Krummel, P. B., Luderer, G., Meinshausen, N., Montzka, S. A., Rayner, P. J., Reimann, S., Smith, S. J., van den Berg, M., Velders, G. J. M., Vollmer, M. K., and Wang, R. H. J.: The shared socio-economic pathway (SSP) greenhouse gas concentrations and their extensions to 2500, Geosci. Model Dev., 13, 3571–3605, https://doi.org/10.5194/gmd-13-3571-2020, 2020.

Mills, M., Richter, J. H., Tilmes, S., Kravitz, B., MacMartin, D. G., Glanville, A. A., Tribbia, J. J., Lamarque, J.-F., Vitt, F., Schmidt, A., Gettelman, A., Hannay, C., Bacmeister, J. T., and Kinnison, D. E.: Radiative and chemical response to interactive stratospheric aerosols in fully coupled CESM1(WACCM), J. Geophys. Res.-Atmos., 122, 13061 13078, https://doi.org/10.1002/2017JD027006, 2017.

Quaglia, I., Visioni, D., Bednarz, E. M., MacMartin, D. G., and Kravitz, B.: The Potential of Stratospheric Aerosol Injection to Reduce the Climatic Risks of Explosive Volcanic Eruptions, Geophysical Research Letters, 51, e2023GL107702, https://doi.org/10.1029/2023GL107702, 2024.

Reinhard, E., Stark, M., Shirley, P., and Ferwerda, J.: Photographic tone reproduction for digital images, ACM Transactions on Graphics, 21, 267–276, https://doi.org/10.1145/566654.566575, 2002.

Rozanov, A. V., Rozanov, V. V., and Burrows, J. P.: Combined differential-integral approach for the radiation field computation in a spherical shell atmosphere: Non-limb geometry, J. Geophys. Res., 105, 22937–22942, https://doi.org/10.1029/2000JD900378, 2000.

Rozanov, V., Rozanov, A., Kokhanovsky, A., and Burrows, J.: Radiative transfer through terrestrial atmosphere and ocean: Software package SCIATRAN, J. Quant. Spectrosc. Ra., 133, 13–71, 2014

Sinnhuber, B. M., Weber, M., Amankwah, A., and Burrows, J. P.: Total ozone during the unusual Antarctic winter of 2002, Geophys. Res. Lett., 30, 1580, https://doi.org/10.1029/2002GL016798, 2003.

Symons, G., Judd, J., Strachey, R., Wharton, W., Evans, F., Russell, F., Archibald, D., and Whipple, G.: The Eruption of Krakatoa: And Subsequent Phenomena, Krakatoa Committee of the Royal Society (Great Britain), Trübner and Co., Ludgate Hill, https://doi.org/10.3931/e-rara-16337, 1888.

von Savigny, C., Lange, A., Hoffmann, C. G., and Rozanov, A.: Explaining the green volcanic sunsets after the 1883 eruption of Krakatoa, Atmos. Chem. Phys., 24, 2415–2422, https://doi.org/10.5194/acp-24-2415-2024, 2024.

Wullenweber, N., Lange, A., Rozanov, A., and von Savigny, C.: On the phenomenon of the blue sun, Clim. Past, 17, 969–983, https://doi.org/10.5194/cp-17-969-2021, 2021.